

Star formation in the outer regions of the early-type galaxy NGC 4203

Mustafa K. Yıldız^{1,2,3*}, Paolo Serra³, Tom A. Oosterloo^{1,4}, Reynier F. Peletier¹,
Raffaella Morganti^{1,4}, Pierre-Alain Duc⁵, Jean-Charles Cuillandre^{5,6}, Emin Karabal^{5,7}

¹*Kapteyn Astronomical Institute, University of Groningen, P. O. Box 800, 9700 AV Groningen Netherlands*

²*Astronomy and Space Sciences Department, Science Faculty, Erciyes University, Kayseri, Turkey*

³*CSIRO Astronomy and Space Science, Australia Telescope National Facility, PO Box 76, Epping, NWS 1710, Australia*

⁴*Netherlands Institute for Radio Astronomy (ASTRON), Postbus 2, 7990 AA Dwingeloo, The Netherlands*

⁵*Laboratoire AIM Paris-Saclay, CEA/Irfu/SAP CNRS Université Paris Diderot, 91191 Gif-sur-Yvette Cedex, France*

⁶*Observatoire de Paris, PSL Research University, France*

⁷*European Southern Observatory, Karl-Schwarzschild-Str. 2, 85748 Garching, Germany*

Submitted 0 August 1234; Accepted 0 October 1234

ABSTRACT

NGC 4203 is a nearby early-type galaxy surrounded by a very large, low-column-density H I disc. In this paper we study the star formation efficiency in the gas disc of NGC 4203 by using the UV, deep optical imaging and infrared data. We confirm that the H I disc consists of two distinct components: an inner star forming ring with radius from ~ 1 to $\sim 3 R_{eff}$, and an outer disc. The outer H I disc is 9 times more massive than the inner H I ring. At the location of the inner H I ring we detect spiral-like structure both in the deep $g' - r'$ image and in the $8 \mu\text{m}$ *Spitzer*-IRAC image, extending in radius up to $\sim 3 R_{eff}$. These two gas components have a different star formation efficiency likely due to the different metallicity and dust content. The inner component has a star formation efficiency very similar to the inner regions of late-type galaxies. Although the outer component has a very low star formation efficiency, it is similar to that of the outer regions of spiral galaxies and dwarfs. We suggest that these differences can be explained with different gas origins for the two components such as stellar mass loss for the inner H I ring and accretion from the inter galactic medium (IGM) for the outer H I disc. The low level star formation efficiency in the outer H I disc is not enough to change the morphology of NGC 4203, making the depletion time of the H I gas much too long.

Key words: galaxies: elliptical and lenticular – galaxies: evolution – galaxies: individual(NGC 4203) – galaxies: ISM – galaxies: structure

1 INTRODUCTION

Although we have long known that early-type galaxies (ETGs) can harbour a stellar disc, their actual distribution of bulge-to-disc ratios B/D has been debated for many decades (e.g., Spitzer & Baade 1951; Sandage, Freeman & Stokes 1970; van den Bergh 1976). Recently, a number of studies based on broad-band imaging and integral-field spectroscopy at optical wavelengths have concluded that most ETGs host a stellar disc, and that ETGs as a family cover a similar range of B/D ratio as spirals (Cappellari et al. 2011; Laurikainen et al. 2011; Kormendy & Bender 2012; Krajnović et al. 2013; Weijmans et al. 2014). Discs are detected also with a number of additional techniques such as narrow-band imaging of emission lines (e.g., H β), imaging of dust absorption, or the observation

of the kinematics of planetary nebulae and globular clusters (Romanowsky et al. 2003; Sarzi et al. 2006; Pota et al. 2013). Taken together, these results suggest that galaxy evolution is dominated by processes which allow the growth and survival of stellar discs in galaxies of both early- and late type.

Discs have also been found in the cold gas phase of ETGs by means of both neutral hydrogen (H I) and CO observations (e.g., van Driel & van Woerden 1991; Young 2002; Morganti et al. 2006; Oosterloo et al. 2007, 2010; Crocker et al. 2011). More recently, ATLAS^{3D} observations of H I and CO have shown that ~ 50 percent of all ETGs contain some cold gas (Young et al. 2011; Serra et al. 2012, hereafter S12). Molecular gas is typically found in small gas discs in the central regions and is linked to small amounts of star formation (Alatalo et al. 2013; Davis et al. 2013). In contrast, in ~ 20 percent of ETGs outside clusters H I has been found distributed in low-column density discs or rings with typical sizes of many tens of kpc, much larger than the stellar body (S12). If the column

* E-mail: mkyildiz@astro.rug.nl

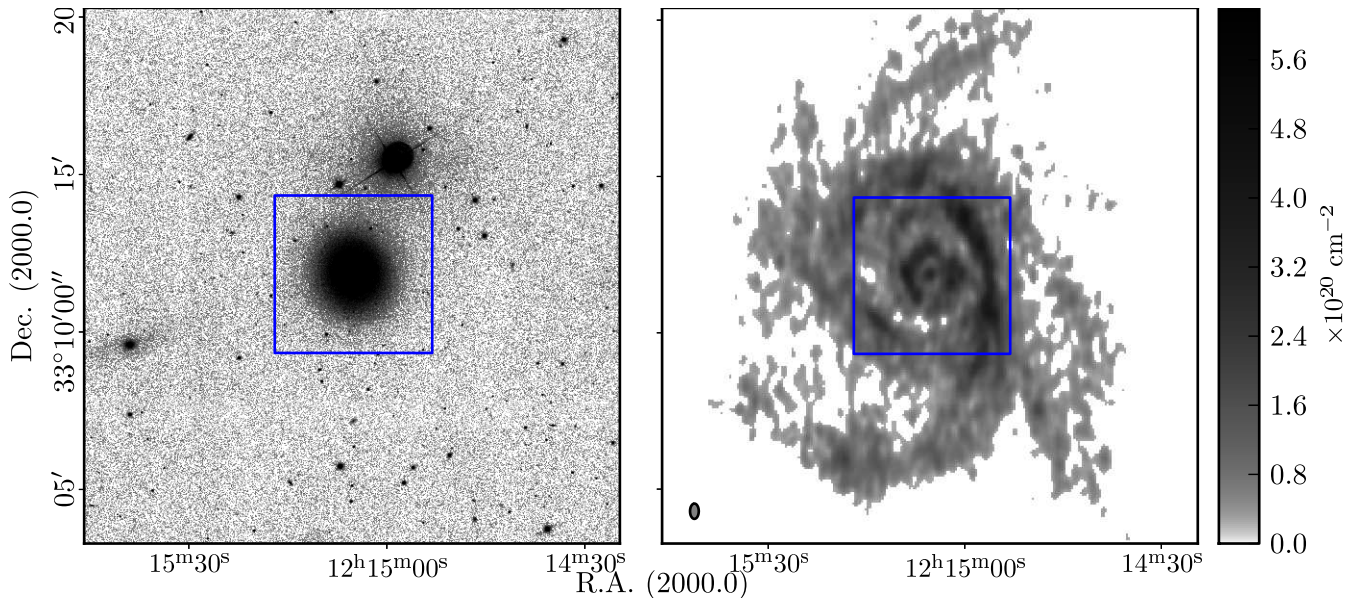


Figure 1. SDSS *g*-band(left) and new deep WSRT H I (right: see Sec. 2.1) images of NGC 4203. The size of the images is $\sim 74 \times 74 \text{kpc}^2$ ($17' \times 17'$). The colourbar refers to the H I image. The H I beam is shown in the bottom-left corner of the H I image. The blue boxes represent the size of the images shown in Fig. 2.

density of the gas is high enough, these H I discs are potential fuel for star formation (SF). Contrary to the general idea that galaxies evolve from late- to early type, these H I reservoirs could generate the growth of stellar discs and therefore trigger the transition of the host from an early- to a late-type morphology (Cortese & Hughes 2009; Fang et al. 2012; Salim et al. 2012).

In this context, many recent studies have focused on the presence of SF in the outer discs of ETGs (Salim & Rich 2010; Lemoias et al. 2011; Moffett et al. 2012; Salim et al. 2012). Such SF is typically traced by UV light emitted by massive stars of age up to several hundreds Myr (Kauffmann et al. 2007; Bianchi 2011; Salim et al. 2012). Moffett et al. (2012) show that ~ 40 percent of 38 red sequence and blue cloud ETGs with stellar mass below $\sim 4 \times 10^{10} M_{\odot}$ have extended UV discs, which is evidence for disc growth in these objects.

In this paper, we aim to bring these two lines of investigation (H I and UV) together and study SF in the large H I disc of the early-type galaxy NGC 4203. This is a nearby, nearly face-on lenticular. Figure 1 shows an SDSS *g*-band image of the galaxy (left panel) and Table 1 provides some basic information. NGC 4203 has been observed at many wavelengths. Optical studies show that NGC 4203 has a relatively massive stellar disc ($B/D = 0.4\text{--}0.5$ – Burstein 1979; Krajnović et al. 2013). Early H I observations revealed a low-column-density H I disc with a complex morphology (Burstein & Krumm 1981; van Driel et al. 1988). More recent observations show that the H I disc extends to very large radius and is characterised by spiral-like H I arms (S12). This gas rotates regularly around the galaxy and is kinematically aligned with the stellar disc (Serra et al. 2014).

Despite the large H I reservoir ($\sim 10^9 M_{\odot}$), the stellar population is uniformly old (~ 10 Gyr) inside $1 R_{\text{eff}}$ (McDermid et al. 2015) suggesting that the H I is not fueling a high level of SF in this region. Yet, there are signs of possible low-level SF within the stellar body. For instance, NGC 4203 contains $2.5 \times 10^7 M_{\odot}$ of H_2 in the centre (Welch & Sage 2003; Young et al. 2011). Hubble Space Telescope observations show nuclear dust structures in the very centre

Table 1. General properties of NGC 4203

Quantity	Value	Unit	Reference
Hubble Type	SAB0	–	(1)
R.A. (J2000)	$12^{\text{h}}15^{\text{m}}05.06^{\text{s}}$	HMS	(2)
Dec. (J2000)	$+33^{\text{d}}11^{\text{m}}50.382^{\text{s}}$	DMS	(2)
Helio. Rad. Vel.	1086 ± 4	km/s	(1)
Distance	14.7	Mpc	(3)
M_K	-23.4	mag	(3)
A_B	0.05	mag	(3)
Effective Radius	29.5	arcsec	(3)
$\log(M/L)_{\text{star}}$	0.5	M_{\odot}/L_{\odot}	(4)
$\log M_{\text{star}}$	10.6	M_{\odot}	(4)
Galactic $E(B - V)$	0.012	mag	(5)

References:(1) de Vaucouleurs et al. (1991); (2) Anderson & Ulvestad (2005) (3) Cappellari et al. (2011); (4)Cappellari et al. (2013); (5) Schlegel, Finkbeiner & Davis (1998);.

of the galaxy (300 pc radius; Erwin & Sparke 2003). The dust is visible also on a large scale in a $8 \mu\text{m}$ image, where the flux, mostly from polycyclic aromatic hydrocarbons (PAHs) appears distributed in a spiral-like pattern (Pahre et al. 2004; we will make use of this image as well as of a $24 \mu\text{m}$ image in support of our analysis of SF in NGC 4203).

Here we use new, deep H I observations and UV imaging from the *Galaxy Evolution Explorer* (GALEX) to study the relation between H I and star formation as well as the impact of this large gas reservoir on NGC 4203. In Section 2 we describe the data (H I, FUV, infrared as well as ancillary optical imaging) and the methodology used for our work. In Section 3 we discuss global properties of the H I, FUV, infrared and optical images, present the derivation of star formation rate (SFR) from the data and compare the SF efficiency in the H I disc with that of late-type and dwarf galaxies. In Section 4 we discuss the origin of the H I gas and its impact on the host galaxy. In Section 5 we give a summary of the work.

2 DATA AND ANALYSIS

2.1 WSRT data reduction

We select NGC 4203 from the sample of ETGs with extended H I discs presented by S12. We observe this galaxy for 9×12 hours using the Westerbork Synthesis Radio Telescope (WSRT). Compared to the original 12-h observation by S12, this longer integration allows us to image the H I down to a similar column density but at a significantly higher angular resolution. This is desirable to compare the H I image to the UV image used to study SF (see below).

We reduce separately the 9 H I datasets (12-h integration each) following standard techniques with the MIRIAD package (Sault, Teuben & Wright 1995). Having calibrated and subtracted the continuum from the datasets, we combine them in the UV plane and image with robust=0.4 weighting, obtaining an H I cube with an angular resolution of 29.3×16.7 arcsec² (PA=0.5 deg). The velocity resolution is 16 km s⁻¹ after Hanning smoothing. The noise level of the data cube is 0.12 mJy beam⁻¹.

We create an H I image by summing flux at all velocities using only pixels included in a mask. In order to include diffuse, faint emission in the mask, we select pixels above a certain threshold in: (i) the original data cube; (ii) four data cubes smoothed spatially with a 2D Gaussian of FWHM 30, 45, 60 and 90 arcsec, respectively; (iii) three data cubes smoothed in velocity with a Hanning filter of width 32, 64 and 112 kms⁻¹; (iv) six data cubes obtained smoothing in velocity the 30- and 60 arcsec resolution cubes as in point (iii). We create the mask using a 3 σ threshold except for the 90-arcsec resolution cube, for which we adopt a 4 σ threshold.

We determine a detection limit from the original data cube as a 5 σ signal in a single velocity resolution element, obtaining 2.3 × 10¹⁹ cm⁻². We obtain the final H I image by applying the WSRT primary beam correction to all pixels above this detection limit in the moment zero image derive from the masked H I cube. We show the H I image in Fig. 1 (right panel) and a zoom in on the central 300 arcsec in Fig. 2 (top-left panel).

2.2 GALEX data reduction

We obtain GALEX UV images of NGC 4203 from the Mikulski Archive for Space Telescopes. We use data from the Calibration Imaging, whose goals and specifications are described in Martin & GALEX Team (2005). The GALEX field of view (FOV) is ~ 1.2 degrees in diameter and the instrument has two main bands: the far-UV (FUV) and the near-UV (NUV). The effective wavelengths for the FUV and NUV channels are 1516Å and 2373Å, with 4.5 arcsec and 6 arcsec resolution (FWHM), respectively. Details can be found in Morrissey et al. (2005, 2007). Our study is mostly based on the FUV data because the FUV emission is more sensitive to recent star formation than the NUV emission (Bianchi 2011).

Since NGC 4203 has not been observed as a target galaxy, the position of the galaxy is different in all the 10 GALEX images. Therefore, we have selected 5 GALEX images where NGC 4203 is sufficiently far from the edge of the GALEX FOV to grant good image quality and reasonable background uniformity. The total exposure time of these 5 UV images is 1186 sec. For the purpose of comparing the distribution of UV emission and H I gas, we analyse a 1500 × 1500 arcsec² GALEX image centered on NGC 4203. Figure 2 shows the central 300 arcsec of the FUV image, which is the only region where emission from SF in the H I disc is clearly visible by eye.

We make use of the SDSS photometric catalogue (Ahn et al.

2012) to mask background and foreground objects based on their type (unresolved or extended), brightness, colour and Petrosian radius. For the unresolved sources we adopt a radius equal to the GALEX point spread function (PSF), otherwise we use the Petrosian radius of the object itself. Following visual inspection of the UV images, we choose to mask the objects with $g' - r' \leq 1$ and 1.5, and with $g \leq 19.5$ and 21.1 mag for the unresolved and resolved sources, respectively. We estimate the local background from the masked images by applying a moving mean filter of size 300 × 300 pixel² (450 × 450 arcsec²). The filtering is performed iteratively by clipping three times at a 4.5 σ level. To avoid over-estimating the background, we mask a large area (300 arcsec diameter) around the centre of the galaxy. We subtract this background from the original, masked image. Additionally, a flat residual background is subtracted from the UV image before proceeding with our analysis (see Sec. 3.3).

Finally, we correct the FUV image for the effect of Galactic extinction. We use an $E(B-V) = 0.012$ based on the dust images by Schlegel, Finkbeiner & Davis (1998) and assume that $A_{FUV} = 8.24 \times E(B-V)$ and $A_{NUV} = 8.2 \times E(B-V)$ (Wyder et al. 2007). Thus, we use the following equations for the Galactic correction:

$$I_{FUV,corr} = I_{FUV} \times 1.1 \quad (1)$$

$$I_{NUV,corr} = I_{NUV} \times 1.08 \quad (2)$$

2.3 Ancillary optical and infrared images

We support our study of SF, which is primarily based on the UV images described above, with ancillary images at 8 μ m, 24 μ m and optical wavelengths. The 8 μ m mid-infrared emission is generally considered to trace the PAHs heated by UV photons (Leger & Puget 1984; Sellgren 1984). It is thought that 2/3 of the 8 μ m emission from a galaxy originates from heating by stellar populations 100 Myr or younger (Calzetti et al. 2005; Calzetti 2013), and that PAH emission is stronger for increasing metallicity and dust content of the interstellar medium (e.g., Engelbracht et al. 2005; Marble et al. 2010; Calzetti 2013). The 24 μ m emission is generally produced by dust following absorption of UV photons emitted by young stars, and traces SF on a time scale of 10 Myr (Calzetti et al. 2005; Leroy et al. 2008).

In this paper we use archival 3.6 μ m, 8 μ m and 24 μ m images from Fazio et al. (2004) obtained with the Infrared Array Camera and The Multiband Imaging Photometer on the *Spitzer Space Telescope* (Rieke et al. 2004; Werner et al. 2004). We remove the background from each image by subtracting the average pixel value calculated in a number of empty regions.

The 8 μ m image includes a contribution from stars in the galaxy, which we remove by subtracting the 3.6 μ m image scaled by a factor $X_{3,6}$ as in Shapiro et al. (2010). These authors find that $X_{3,6}$ has very low scatter about a median value of 0.264 for ETGs, and we adopt this value for NGC 4203. The bottom-left panel of Fig. 2 shows the resulting 8 μ m-non stellar image. Similarly, the 24 μ m flux is also contaminated by emission from old stellar populations and hot, circumstellar dust (e.g., Salim et al. 2009; Kelson & Holden 2010; Martini, Dicken & Storchi-Bergmann 2013). To remove this emission, we apply the same scaling method used for the 8 μ m. We have adopted a scaling factor from Martini, Dicken & Storchi-Bergmann (2013) that study the empirical 24 μ m scaling factor for dust-free ETGs.

We also use deep optical images of NGC 4203 that are obtained in the g' and r' bands using the MegaCam camera on the Canada-France-Hawaii Telescope. These observations are obtained

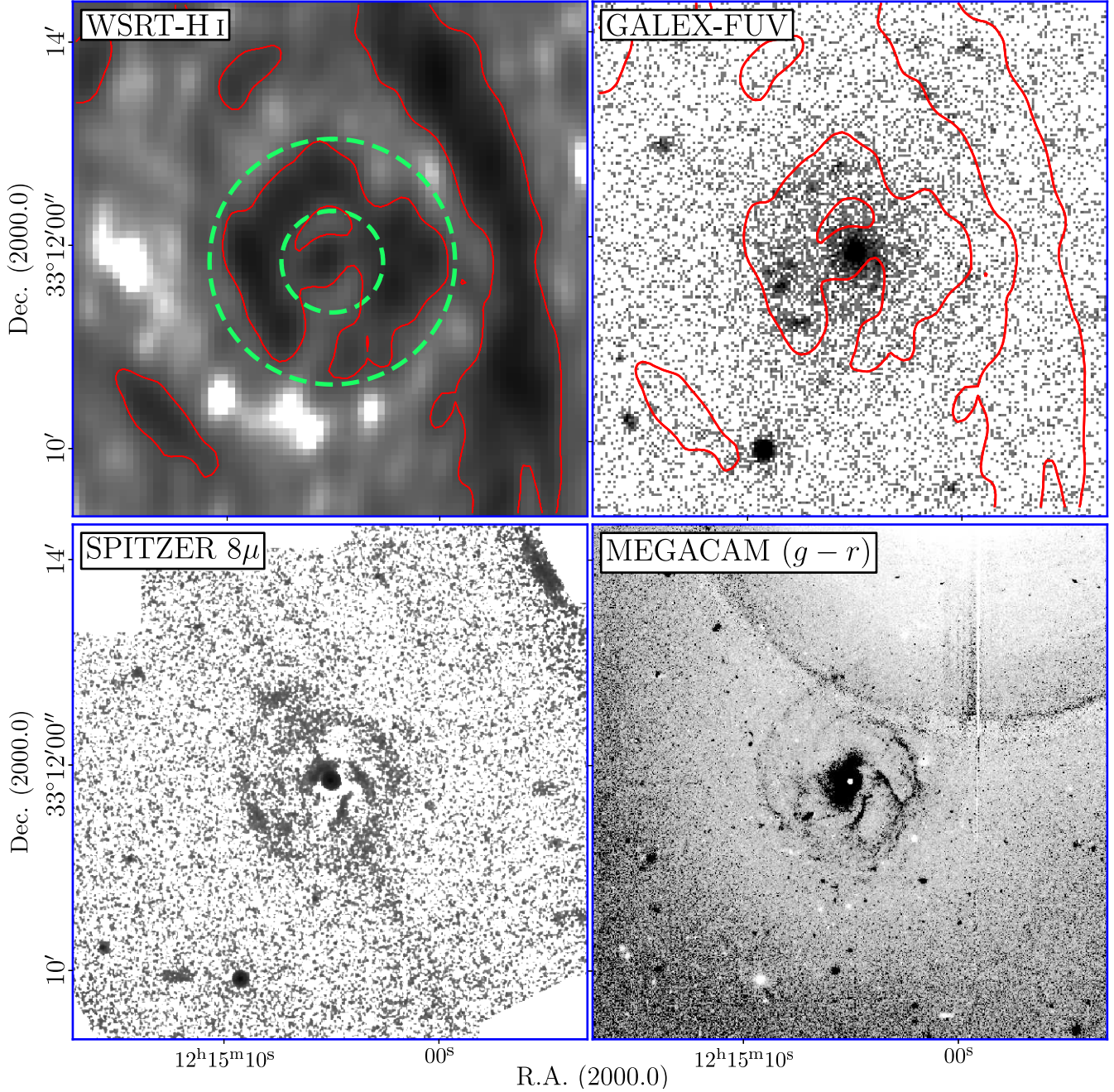


Figure 2. Zoomed-in images of the deep H I (top-left), GALEX-FUV (top-right), Spitzer 8μ infrared (bottom-left) and deep MegaCam $g' - r'$ colour (bottom-right) images. All images show a field of size $300'' \times 300''$ ($\sim 22\text{kpc} \times 22\text{kpc}$). Dark areas correspond to redder regions in the deep MegaCam colour image. The red contours on the H I and FUV images represent an H I column density of $1.8 \times 10^{20} \text{ cm}^{-2}$. The location of the inner H I ring is shown by the green-dashed lines.

as part of the MATLAS / ATLAS^{3D} Large Program. The observing strategy and data reduction procedures with the LSB-Elixir pipeline optimized for the detection of extended low surface brightness features are described in Duc et al. (2015). Further processing is carried out to remove the extended artificial halos surrounding two nearby bright stars. We determine the stellar PSFs, including their extended wings, with a manual procedure (as explained in Duc et al. 2015). On the resulting image (see Fig. 3, top), the early type galaxy exhibits a rather regular extended outer stellar halo, and a dwarf galaxy can be seen east of NGC 4203.

We compute a model of the NGC 4203 with the ellipse fitting procedure of IRAF for both the g' and r' band images and then subtract these models from the original images. The resulting residual image together with the g' band image of the dwarf galaxy is shown at the bottom panel of Fig. 3, and it is obvious that some extended spiral/ring structures show up in the main body of the lenticular galaxy.

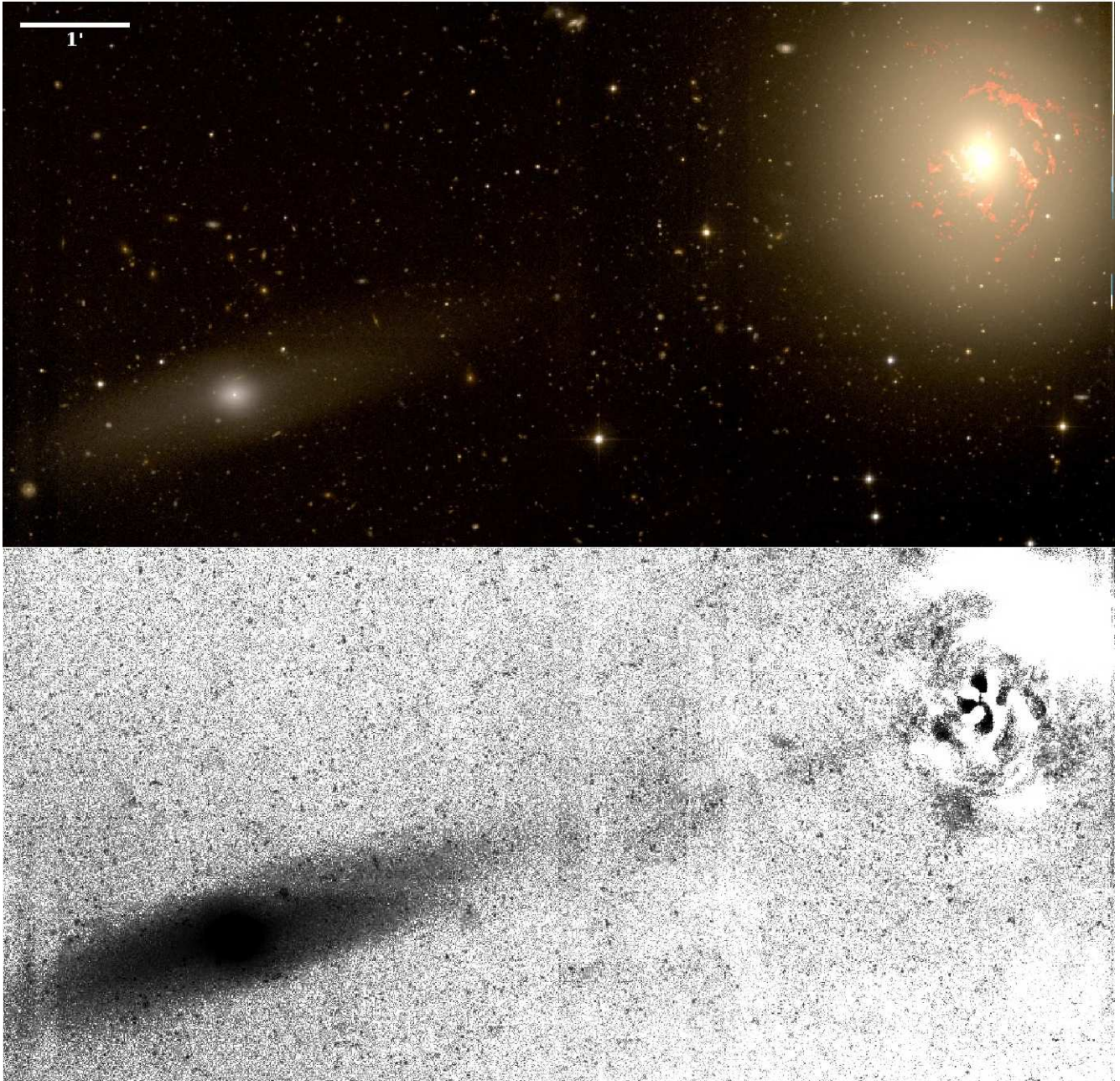


Figure 3. *Top:* Composite $g' + r'$ Megacam image of NGC 4203 with the dust lanes superimposed in red. The dust lanes are obtained by summing the residual $g' + r'$ images after a galaxy model subtraction (see Sec. 2.3). This image also shows the disrupted companion dwarf galaxy at the east of the galaxy. *Bottom:* MegaCam g' band image of the disrupted companion dwarf galaxy and residual map of NGC 4203. It exhibits a possible faint tail East of our galaxy which as the same direction as the two tidal tails of the companion dwarf (see Sec. 3.1). The white bar shows a length of 1 arcmin.

2.4 SFR calculation

We estimate the SFR using the various tracers described above (FUV, non-stellar $8 \mu\text{m}$ and $24 \mu\text{m}$). In order to convert FUV emission into SFR we use a conversion from Bigiel et al. (2010),

$$\Sigma_{\text{SFR}} [\text{M}_{\odot} \text{yr}^{-1} \text{kpc}^{-2}] = 0.68 \times 10^{-28} \times I_{\text{FUV}} [\text{erg s}^{-1} \text{Hz}^{-1} \text{kpc}^{-2}], \quad (3)$$

where I_{FUV} is the FUV intensity per unit area and the initial mass function (IMF) is assumed to be of a Kroupa type. This estimate could in principle be corrected for internal extinction on the basis of the H I image using the relation $N(\text{H I})/E(B - V) = 5 \times 10^{21} \text{cm}^{-2} \text{mag}^{-1}$ presented by Bohlin, Savage & Drake (1978). This re-

lation is derived for the Milky Way and therefore is likely to provide an upper limit on the extinction in metal poor environments. In the case of NGC 4203, the peak H I column density is $\sim 4.5 \times 10^{20} \text{cm}^{-2}$ and, thus, the maximum extinction should be around ~ 25 percent. In the outer regions, where the H I column density is much lower ($\sim 3 \times 10^{19} \text{cm}^{-2}$), the extinction decreases to a negligible ~ 2 percent. In this paper we do not apply this correction but instead trace SF in dusty environments by using infrared imaging.

Although we do not expect a large amount of dust in the outer regions of NGC 4203, Fig. 2 shows that in the inner regions dust is present and this will affect the calculation of SFR. As mentioned

in Section 2.3, the FUV emission absorbed by dust is re-emitted at infrared wavelengths. We use the conversion from Wu et al. (2005) to estimate SFR from the $8\ \mu\text{m}$ non-stellar image:

$$\Sigma_{\text{SFR}}[\text{M}_{\odot}\text{yr}^{-1}\text{kpc}^{-2}] = 8.43 \times 10^{-3} I_{8\mu\text{m}}(\text{non stellar}), \quad (4)$$

where $I_{8\mu\text{m}}$ is the non-stellar $8\ \mu\text{m}$ intensity in MJy ster^{-1} .

We also combine the FUV and non-stellar $24\ \mu\text{m}$ images to estimate the SFR as in Leroy et al. (2008):

$$\Sigma_{\text{SFR}}[\text{M}_{\odot}\text{yr}^{-1}\text{kpc}^{-2}] = 8.1 \times 10^{-2} I_{\text{FUV}} + 3.2 \times 10^{-3} I_{24\mu\text{m}}(\text{non stellar}), \quad (5)$$

where I_{FUV} and I_{24} are in MJy ster^{-1} , and similar to Eq. 3 a Kroupa type IMF is used.

Below we study the SF at the original resolution of the FUV and infrared images as well as at the resolution of the H I image in order to compare the distribution of neutral gas and SFR.

3 GLOBAL PROPERTIES OF FUV, H I, AND ANCILLARY IMAGES

3.1 Flux distribution of the images

Early studies emphasize that the H I properties of NGC 4203 are similar to those of spiral galaxies. For example, Burstein & Krumm (1981) and van Driel et al. (1988) find a distorted rotation curve from the H I velocity field, possibly suggesting an oval distortion or a kinematical warp (Bosma 1978). They find that the H I disc is 3 times larger than the optical body and this is confirmed later by S12 using deeper data.

As described in Section 2, our new H I image has similar sensitivity as that of S12 but a much better resolution. We detect H I down to a column density of $2.3 \times 10^{19}\ \text{cm}^{-2}$ at a resolution of $29.3 \times 16.7\ \text{arcsec}^2$. Using the new H I observations, one can easily see a dense gas ring whose size is similar to that of the stellar body (Fig. 1). This ring is embedded in a much larger H I disc characterised by long spiral-like arms. The H I disc extends out to $\sim 40\ \text{kpc}$ from the galaxy centre and contains ~ 9 times more H I gas than the inner ring. Table 2 lists some basic galaxy properties derived from the H I image.

3.2 Impact of the H I on the host galaxy

Figure 2 shows that NGC 4203 hosts some diffuse FUV emission at the location of the inner H I ring. Additionally, at the same location, we see spiral-like structure in both the $8\ \mu\text{m}$ and $g' - r'$ images, which is clumpy and almost identical in these images. Moreover, the extended spiral/ring structures in the model subtracted deep optical image (bottom panel of Fig. 3) correspond to the dust lanes visible in the MegaCam $g' - r'$ colour image.

In contrast, the bright H I arm $\sim 2\ \text{arcmin}$ west of the galaxy (visible in the same figure and referred to as western H I arm in the rest of this paper) does not exhibit any clear FUV emission. A similar picture is evident from the $8\ \mu\text{m}$ -non stellar image and the $g' - r'$ image. While there is clear emission from PAHs and dust absorption in the H I ring, these features are absent from the region occupied by the western H I arm. The question is why these two regions have such different levels of the FUV and $8\ \mu\text{m}$ emission despite the very similar H I column density. We will come back to this point in Sec 4.1.

As indicated in Sec. 2.3, the deep optical images show a dwarf satellite $\sim 7.2\ \text{arcmin}$ (32 kpc) east of the NGC 4203. This dwarf is red and at a similar redshift with $V_{\text{helio}} = 1067 \pm 24\ \text{kms}^{-1}$

Table 2. Observational results for NGC 4203

Quantity	Value	Unit	\pm b,c,d
$\log M(\text{H I})$	9.12	M_{\odot}	2 %
$\log M(\text{H I})_{\text{Ring}}$	8.12	M_{\odot}	5 %
$\log M(\text{H I})_{\text{Disc}}$	9.07	M_{\odot}	2 %
$\log[M(\text{H I})/M_{\text{stellar}}]$	-1.442	–	–
FUV ^a	16.10	ABmag	0.05
FUV(R<100 ^b)	16.92	ABmag	0.06
$\text{SFR}_{\text{Ring},8\mu\text{m}}$	8.4×10^{-3}	$\text{M}_{\odot}\ \text{yr}^{-1}$	3.0×10^{-3}
$\text{SFR}_{\text{Ring},\text{FUV}+24\mu\text{m}}$	4.3×10^{-3}	$\text{M}_{\odot}\ \text{yr}^{-1}$	2.0×10^{-3}
$\text{SFR}_{\text{Ring},\text{FUV}}$	3.8×10^{-3}	$\text{M}_{\odot}\ \text{yr}^{-1}$	1.0×10^{-3}
SFR_{Disc}	9.0×10^{-4}	$\text{M}_{\odot}\ \text{yr}^{-1}$	4.0×10^{-4}
$\text{SFR}_{\text{Ring}+\text{Disc},\text{FUV}}$	4.7×10^{-3}	$\text{M}_{\odot}\ \text{yr}^{-1}$	1.0×10^{-3}
$\bar{\Sigma} \text{SFR}_{\text{Ring}+\text{Disc},\text{FUV}}$	5.9×10^{-5}	$\text{M}_{\odot}\ \text{yr}^{-1}\text{kpc}^{-2}$	1.3×10^{-5}

Note:

^a We take into account the Galactic extinction correction for all the values below. Look at the text for the details.

^b The errors are in the same unit as the values.

^c The errors in H I mass values are derived from the noise level (1σ) of the mask file that is used to create the H I image. We use an annulus that has the same size of the H I beam.

^d The errors in the SFR and FUV magnitude values are calculated from the uncertainties in the photometric measurements of the FUV, $8\ \mu\text{m}$ and $24\ \mu\text{m}$ images (Calzetti et al. 2007; Morrissey et al. 2007; Leroy et al. 2008).

(Adelman-McCarthy et al. 2007). The stellar mass of the dwarf is roughly $\sim 10^8\ \text{M}_{\odot}$ from the SDSS-*i* band photometry.

The bottom panel of Fig. 3 reveals prominent tidal tails associated to the dwarf and a faint stream, which has the same direction as these tidal tails. From this point, it is clear that the satellite dwarf galaxy is interacting with NGC 4203, for example, these features may be associated with a single on-going minor merger event. We will discuss this point in Sec. 4.2.

3.3 H I, FUV and infrared radial profiles

We derive the radial profile of H I, UV and infrared emission along circular annuli whose width increases logarithmically from inside out. The inner region of the radial profiles ($1\ R_{\text{eff}}$) is contaminated by old stars in the bulge and, therefore, we do not include it in our SFR calculation.

Figure 5 shows the resulting H I and UV radial profiles together. The first peak of the H I profile indicates the location of the inner H I ring $\sim 30\text{-}80\ \text{arcsec}$ from the centre. We find that the slope of the declining FUV profile becomes flatter in this region consistent with the presence of diffuse FUV emission associated with the star formation (see Fig. 2). Additionally, the FUV-NUV colour becomes significantly bluer at the same location. This might be because the young stellar populations are dominant in this region. The second peak in the H I profile of Fig. 5 ($\sim 120\text{-}150\ \text{arcsec}$) is caused by the high column density gas in the western H I arm (see Fig. 2). Unlike for the first peak of the H I profile, here the FUV profile does not seem to depart from the general declining trend. However, the FUV-NUV colour seems to become bluer at this location. The most significant diffuse FUV emission in NGC 4203 comes from a region close to the UV-bright galaxy bulge. The emission from the bulge may contaminate a large region around it because the GALEX PSF is characterized by broad wings out to at least $60\ \text{arcsec}$. To quantify this effect we create a bulge model with a Sérsic surface brightness profile and convolve it with the FUV PSF. We

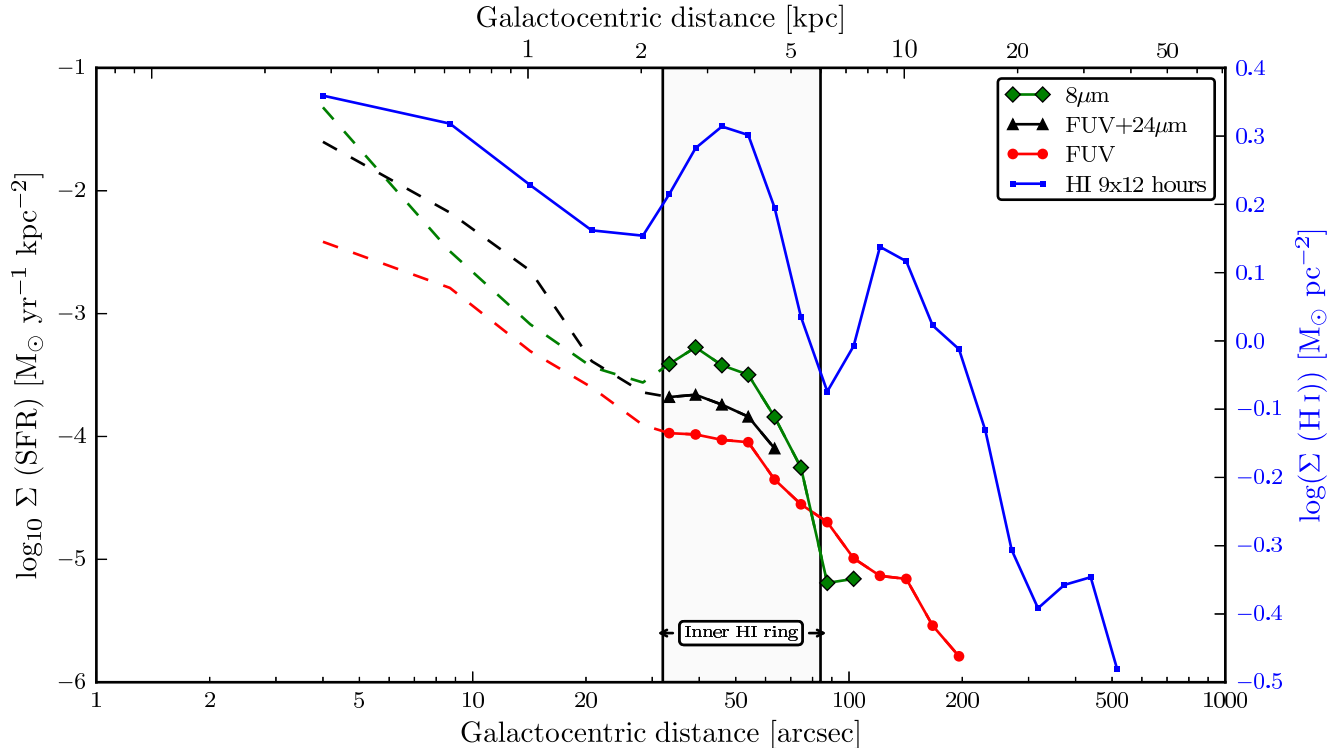


Figure 4. Comparison of different SFR radial profiles together with the H I profile. We calculate the SFR with Eqs. 3, 4 and 5. Although, we show the central emission from all the bands, we do not include these emissions in our SFR calculation. The dashed part of the profiles traces emission from the bulge and this is not included the calculation of SFR in the rest of paper. The gray shaded area and H I profile are the same as in Fig. 5.

find that the average contamination from the bulge is ~ 29.2 AB-mag arcsec $^{-2}$ between 50 and 60 arcsec. This contribution to the total emission is very low and we ignore this effect in our SFR calculation.

In order to take into account the significant $8 \mu\text{m}$ non-stellar emission in the inner H I ring (see Fig. 2), we derive the SFR radial profiles based on this $8 \mu\text{m}$ emission as well as the $24 \mu\text{m}$ emission (see Sec. 2.3 and Eqs. 4 and 5). We show the resulting SFR radial profiles together with the FUV one in Fig. 4. All profiles show a similar trend as their slope changes at the location of the H I ring (in fact, at $8 \mu\text{m}$ the profile increases significantly between 30 and 60 arcsec). The infrared based SFR profiles are up to a factor ~ 3 higher than the profile based on the FUV emission alone. This difference is larger than the errors in the photometric measurements and is likely due to infrared emission from obscured star formation. The photometric uncertainty for the *Spitzer* 8 and $24 \mu\text{m}$ images is \sim a factor of 2, and this uncertainty is also similar for the FUV measurements (Calzetti et al. 2007; Salim et al. 2007). However, at present, the depth of the *Spitzer* images and the small FOV imply that the UV images are the only reliable tracer of SF at larger radius. Table 2 shows the SFR efficiencies at the location of the inner H I ring for all 3 tracers as well as their approximate uncertainties.

3.4 SFR in terms of H I column density

In Fig. 6 we compare H I and SFR surface density by plotting the H I and FUV radial profiles of Fig. 4 against one another. In this figure points are colour-coded according to the distance from the galaxy centre. The reason that the track described by our measurements is not monotonic is the result of the two H I peaks (one corresponding

to the inner H I ring and the other to the outer H I arm; see Figs. 2 and 5) while the UV radial profile decreases monotonically with radius. For comparison, the yellow area shows the spatially resolved relation between H I and SFR surface density inside r_{25} for a sample of nearby ($D < 12$ Mpc) spirals covering a range of morphologies (Bigiel et al. 2008). In this inner region, interstellar medium of these galaxies is dominated by molecular hydrogen. The green vertically and horizontally shaded areas show the same relation for the outer parts (i.e., $1-2 \times r_{25}$) of dwarf and spiral galaxies, respectively (Bigiel et al. 2010). Details about their sample, e.g., the THINGS sample, are given in Walter et al. (2008). This figure shows that the SF efficiency in the bright H I ring around NGC 4203 is consistent with that of late-type galaxies. Moreover, the SF efficiency in the outer regions of NGC 4203 is also consistent with that of outer regions of spiral and dwarf galaxies.

So far we have compared H I and SFR surface density at fixed radius. Below, we perform a pixel by pixel comparison as implemented by previous authors (e.g., Bigiel et al. 2008, 2010; Boissier et al. 2012). To do so, we smooth and re-grid the FUV and infrared images to the resolution and coordinate grid of the H I image. We find this comparison to be characterised by a very large scatter. For this reason, we bin the points along the HI column density axis, and show the average SFR surface density of each bin as well as the scatter in Fig. 7.

This plot shows a weak trend between H I and SFR surface density as well as a large scatter, represented by the blue bars. This large variation of SF efficiency at fixed H I column density is also clear when one compares the H I ring and the western H I arm mentioned above. The green asterisks and red pentagon indicate the average values of SFR surface density and H I column density in

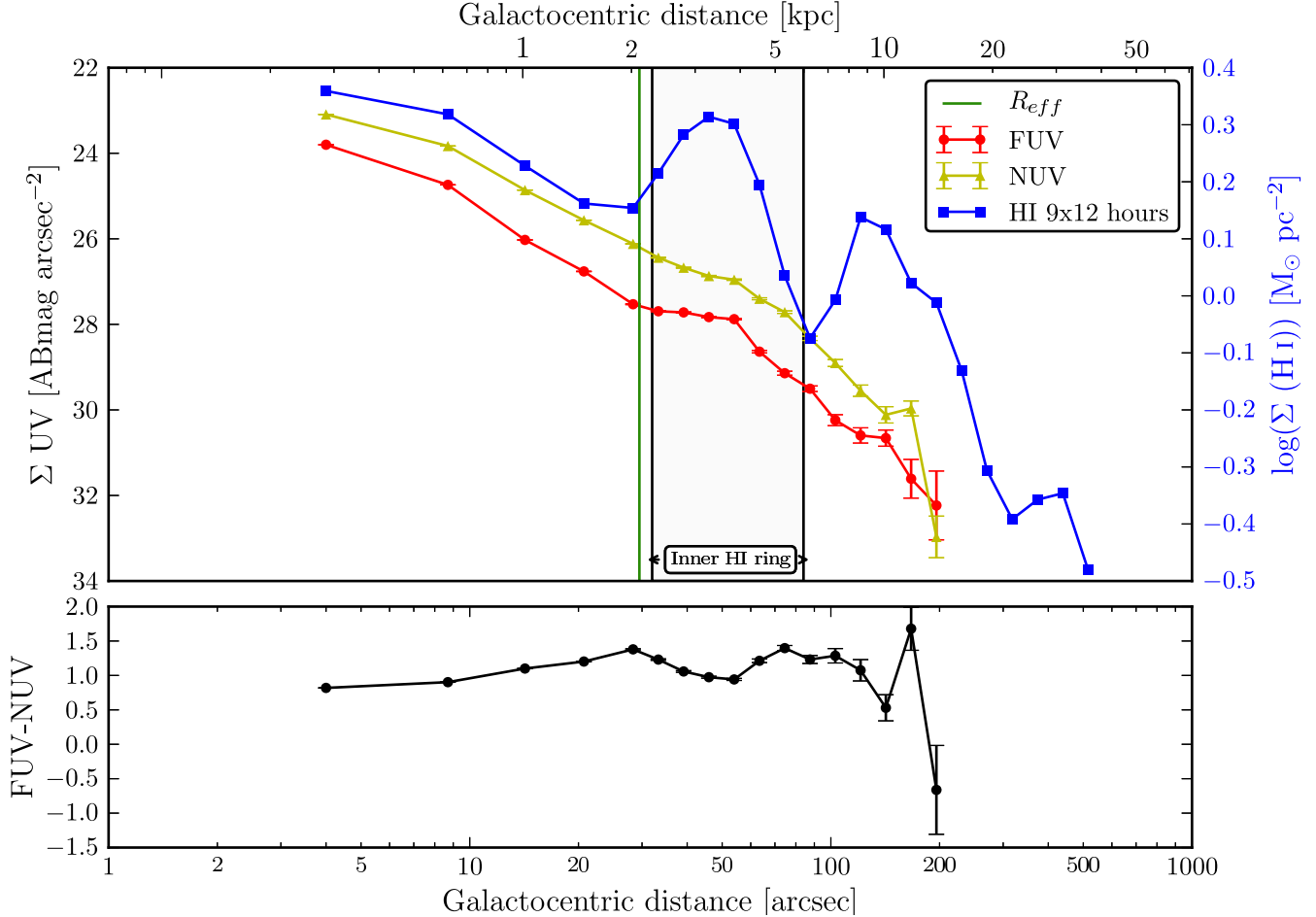


Figure 5. *Top panel:* Radial profiles of the H I (blue) FUV (red) and NUV (yellow) emission. The left y-axis shows the UV magnitude and the right y-axis shows the H I surface density. The green-vertical line shows the effective radius of the galaxy. The gray-shaded region indicates the inner H I ring. *Bottom:* Radial FUV-NUV colour profile. The error bars represent the uncertainty in determining the background for both images.

these two regions, respectively, and are calculated on the basis of the FUV image. Combining the 24 μ m image with the FUV image, the SFR estimate increases further, as illustrated by the first green line. If we calculate the SFR with the 8 μ m non-stellar emission, we obtain the value that is indicated by the second green bar. As argued above, this strengthens our claim that SF efficiency in the inner H I ring is as high as that of spiral galaxies, while it is much lower in the western H I arm despite the similar gas density. However, we note that even if the SFR is low in the western H I arm, this SFR is still consistent with the outer regions of spirals and dwarf galaxies.

4 DISCUSSION

4.1 Star formation efficiency

The previous section demonstrates that at any given H I column density there is a large range of SFR surface densities and, therefore, SF efficiencies in the H I disc of NGC 4203. This is highlighted by the comparison between the H I ring and the western H I arm presented in Fig. 7. There are a number of possible explanations for the difference between these two regions: (i) there may be no direct relation between H I and SF; (ii) the H I column density of the arm might appear to be higher because of projection effects

(e.g., the H I arm stretches away from the plane of the disc), and the actual density of the gas could be too low to form stars; (iii) the temperature of the H I in the arm may be higher than in the ring, making it more difficult to form stars; (iv) The metallicity and dust content of the inner and outer regions might be different due to a difference in formation processes; (v) the western H I arm may be stable against gravitational instabilities, preventing the formation of stars.

Both the second and third points would result in a broadening of the H I spectral profile at the location of the H I arm. This is, however, not observed, leaving us with no clear indication in favour of these options. On the other hand, the fourth point seems an attractive explanation. Miller, Knezek & Bregman (1999) observe a quasar ~ 2 arcmin South-East of the galaxy. Interestingly, they detect one of the closest known damped Ly α (DLA) system. This DLA system belongs to NGC 4203, and the metallicity of the gas to be $[\text{Fe}/\text{H}] = -2.29 \pm 0.1$. They also show a number of heavy-element abundances such as $[\text{Mn}/\text{H}] < -0.68$ and $[\text{Mg}/\text{H}] > -2.4$, respectively. The velocity of the lines are identical to that of the H I emission from the disc of NGC 4203 at the position of the quasar within (± 10 km s⁻¹). Although the metal abundance values are very low, the depletion of the heavy elements onto small dust grains can affect the observed measurements. Vladilo (2002), for instance, show that the corrected $[\text{Fe}/\text{H}]$ abundance of a DLA sys-

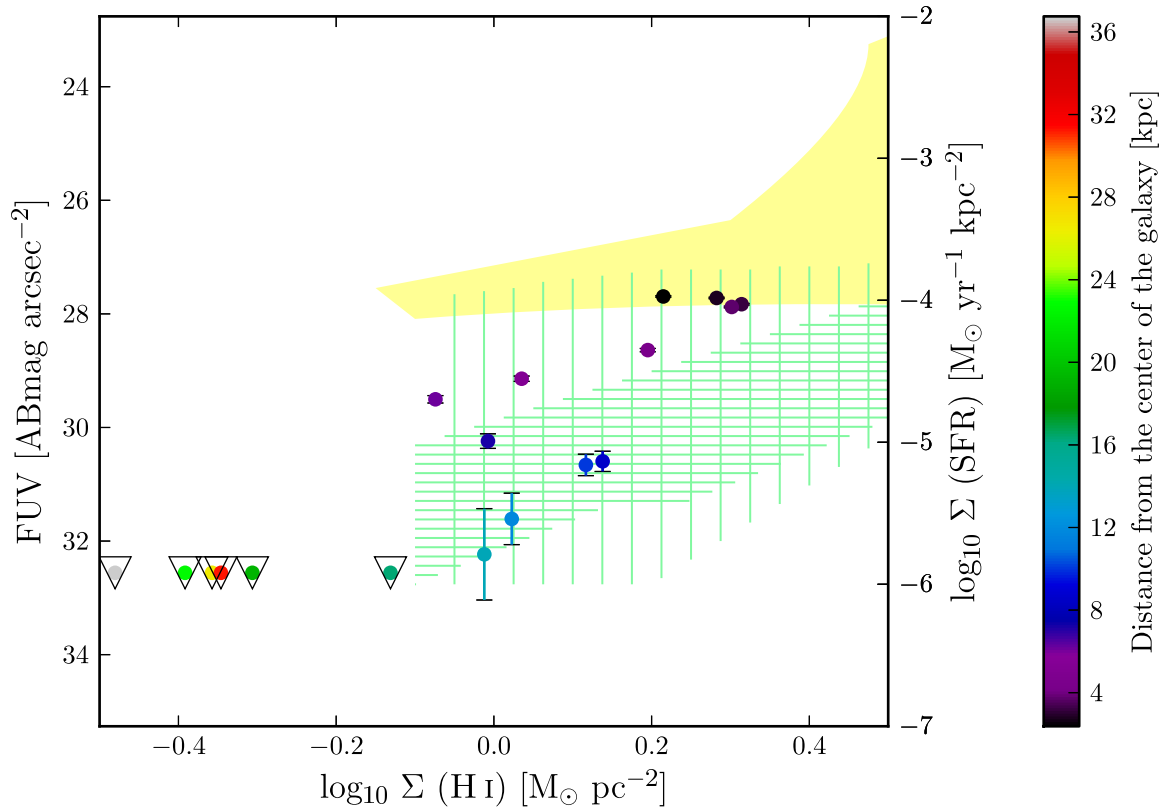


Figure 6. Comparison between H I and FUV surface brightness obtained plotting the radial profiles of Fig. 5 against one another. The triangles indicate H I detected regions with no detectable FUV emission, we estimate the upper limit as equal to the r.m.s. of the FUV background image. The colour bar shows the distance from the centre of the galaxy. The yellow area shows the relation between H I and SFR in the sample of late-type galaxies of Bigiel et al. (2008). The vertical and horizontal green-shaded areas show the location of dwarf galaxies and outer regions of spirals, respectively (Bigiel et al. 2010). In this Figure, the left axis shows the FUV surface brightness and the right axis shows the SFR calculated with Eq. 3.

tem can be on average 0.5 dex (in some extreme cases 1 dex) higher than that of observed. Even if we consider 1 dex depletion effect, the metallicity of the outer H I disc remains very low (i.e., $[\text{Fe}/\text{H}] \sim -1.29$).

This is likely quite different from the inner H I ring, which is known to contain a considerable amount of dust (Fig. 2). In particular, we know that the PAH molecules traced by the $8 \mu\text{m}$ emission are vulnerable to highly energetic photons in dust poor environments due to low dust shielding (e.g., Boselli, Lequeux & Gavazzi 2004; Calzetti et al. 2005), and the PAH emission generally vanishes in regions with metallicity below solar (Engelbracht et al. 2005). Thus the metallicity in the inner region should be significantly higher than in the outer regions. Consequently, different formation processes for the inner and outer H I regions can explain these different metallicities.

The last possibility is the differences of the gravitational instabilities of the H I gas in the inner and outer regions. For example, star formation can occur in regions where the gas disc is unstable against large-scale collapse. If the gas is stable against it, Coriolis forces counteract the self-gravity of the gas and suppress star formation (Leroy et al. 2008, and references therein). This might explain the different SF efficiencies. However, in order to understand this effect, we need further investigation.

4.2 Origin of the H I gas

There are different scenarios that could explain the origin of the H I disc of NGC 4203. One possibility is a high-angular-momentum, gas-rich major merger. Such a merger could result in the formation of a large gas disc (e.g., Barnes 2002). At the same time, it would not necessarily trigger the central burst of SF usually thought to occur during mergers (e.g., Di Matteo et al. 2007; Serra et al. 2008), as evidenced by the old stellar populations in the centre of NGC 4203. If this scenario is correct, we should be able to see a residual from the major merger close to the centre, or a distortion in the outer stellar halo of NGC 4203 in the deep optical image. However, we do not detect any of these features in Fig. 3. Another problem with the major merger scenario is the extremely low metallicity of the outer disc which may rule out that the H I once belonged to a large galaxy.

The other possibility is that the gas has been accreted from the inter-galactic medium. The disturbed appearance of the H I disc may be explained by some minor interaction with a satellite. Indeed, as explained in Sec. 3.1, there is a nearby dwarf satellite, which is most likely interacting with our galaxy. Although this dwarf is positioned at the end of one of the H I arms of NGC 4203 (Fig. 1), we do not detect any H I emission at that position and, therefore, rule out that it is the donor of the H I gas.

However, there is another possibility that this gas can be captured from another gas-rich dwarf galaxy in a single encounter. Since the H I disc is almost regular, this event would happen at

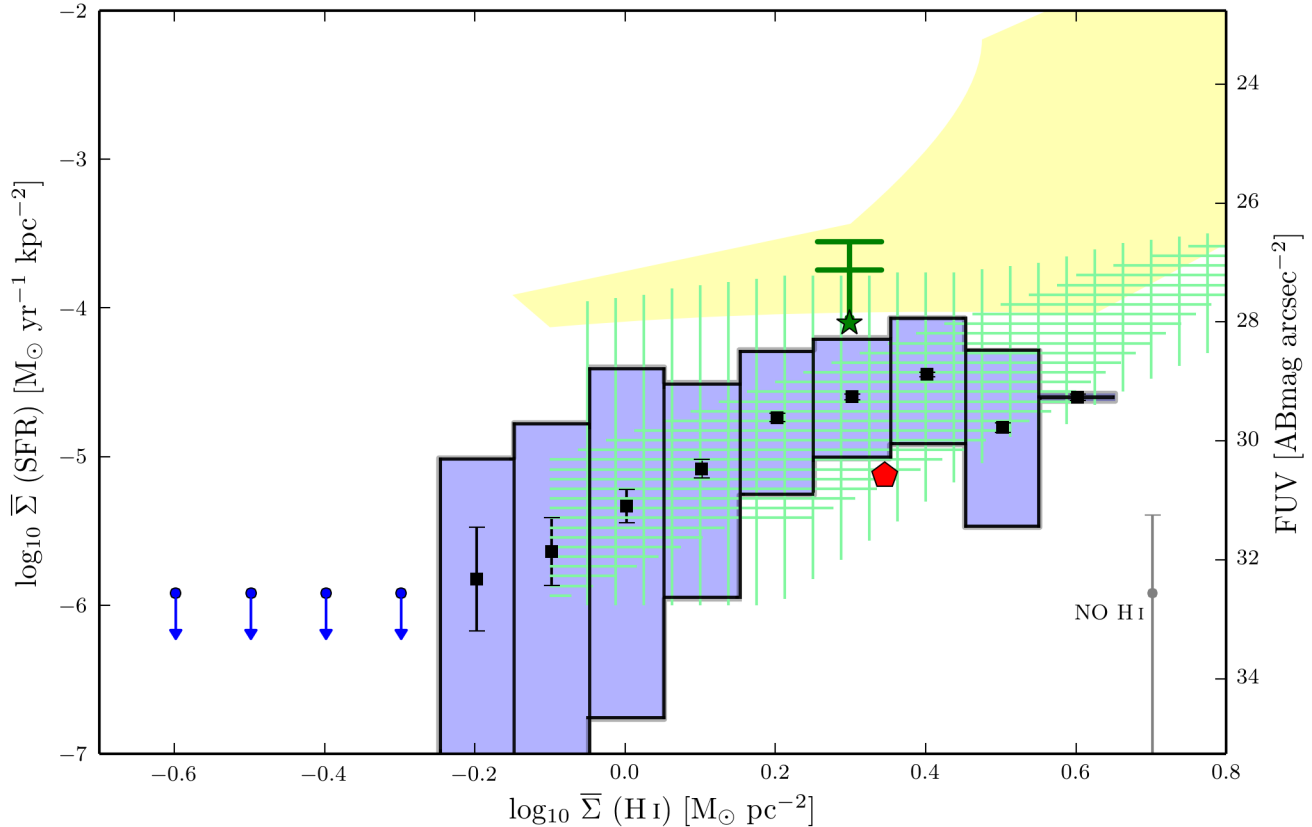


Figure 7. SFR surface density as a function of H I column density based on the pixel by pixel method. Here, the FUV pixels are binned as a function of H I column density. The light blue-shaded area shows the scatter of FUV pixels in the bins. The error bars are similar to those in Fig. 5 and represent the uncertainty in determining the background. The gray error bar on the bottom-right shows the result of same analysis for all the pixels without H I emission. The green asterisk and red pentagon show the inner H I ring and the western H I arm, respectively. The two green lines above the green asterisk represent the SFRs in the inner H I ring that are calculated from Eq. 5 (for FUV+24 μm) and 4 (for 8 μm), respectively. The blue points represent the upper limits, calculated by using the r.m.s. of the FUV background image. The yellow area and green lines are the same as in Figure 6.

least a couple Gyr ago, making it difficult to detect. This is consistent with the conclusion of van Driel et al. (1988) based on a study of the environment around the galaxy.

In conclusion, accretion from the inter-galactic medium would explain the low metallicity of the outer disc, while the inner H I ring may have been enriched of metals by stellar mass loss in the galaxy. Moreover, the disturbed appearance of the outer disc can be explained by an interaction with the satellite visible in Fig. 1 and 3.

We have long known that a large fraction of all ETGs host low levels of on-going or recent SF. This SF activity is detected in their centre using optical spectroscopy (e.g., Trager et al. 2000) or UV photometry (e.g., Yi et al. 2005). Similar to extended-UV discs in late-type galaxies, star formation can also be detected at large radius in early-type galaxies using UV and deep optical imaging (e.g., Salim & Rich 2010; Salim et al. 2012; Fang et al. 2012; Duc et al. 2015). In a few cases it has been possible to establish a link between the presence of H I and SF at the outskirts of ETGs (e.g., Cortese & Hughes 2009; Donovan et al. 2009; Thilker et al. 2010; Duc et al. 2014). Here we explore such link for NGC 4203, and in this section we quantify the impact that the SF hosted within the H I disc has on the morphology of the host.

Table 2 shows the result of our SFR calculation based on the various tracers discussed above, and performed separately for the inner H I ring and the remaining, outer H I disc. In particular, the inner H I ring hosts a significant amount of dust-obscured SF, and

the SFR is best estimated using a combination of 24 μm and FUV emission.

The inner H I ring and outer H I disc are very different from each other. The former contains only ~ 10 percent of the total H I mass but hosts ~ 97 percent of the total SF. The latter hosts the remaining ~ 90 percent of the H I mass but only ~ 3 percent of the total SF. As a result the H I depletion time is much longer in the outer disc ($\sim 10^3$ Gyr) than in the inner H I ring (~ 5 Gyr). If nothing happens to the galaxy, the H I disc could survive for hundreds of a Hubble time at the current SFR.

Overall, the detected amount of SF has a negligible effect on the stellar disc growth and, therefore, the morphology of NGC 4203. Based on the total stellar mass reported by Cappellari et al. (2013) and on the B/D ratio given in Krajnović et al. (2013), the mass of the stellar disc is $\sim 2.7 \times 10^{10} M_{\odot}$. At the current SFR, this mass would grow by a mere 0.1 percent in 1 Gyr. The star formation rate per unit stellar mass in the stellar disc is of just $\sim 10^{-12} \text{ yr}^{-1}$.

If we suddenly convert all the gas in the outer H I disc of NGC 4203 to stars, the R band surface brightness of this region would be 26.8 mag arcsec $^{-2}$. This is ~ 2 magnitude lower than Malin 1, a giant low surface brightness galaxy that has a low surface brightness and very large H I disc (Lelli, Fraternali & Sancisi 2010). In conclusion it is unlikely that NGC 4203 will become a galaxy similar to Malin 1.

5 CONCLUSIONS

NGC 4203 has an H I disc that consists of two separate components. The first component is the inner star forming H I ring. This ring contains metal-rich gas and a large amount of dust. The SF efficiency in the H I ring is comparable to that of inner regions of spiral galaxies and the H I depletion time is of the order of a few Gyr. The second component is the outer H I disc, where the metallicity is likely to be low. The SF efficiency in this disc is much lower than that of centre of spirals even when the H I column density is high (e.g., in the western H I arm) and the H I depletion time is of 100's of the Hubble time. However, the SF efficiency in the outer H I disc is still consistent with that of the outer regions of spiral galaxies and dwarfs.

These two components of the H I structure may be formed in different ways. On the one hand, the H I ring is most likely enriched by stellar processes within the galaxy. On the other hand, the outer H I disc might be accreted from the low metallicity IGM because the outer disc is formed with metal-poor, high column density gas and we cannot find a suitable donor. Subsequent interaction with satellites, which is possibly on-going, may explain the current distorted morphology of the H I disc.

We also detect spiral-like structure in the $8\ \mu\text{m}$ and deep $g' - r'$ images. These spiral-like structure is extending to 3 effective radii ($\sim 6\text{kpc}$), and, because of its clumpiness, is likely organized by the star formation process.

Finally, despite the large H I reservoir and the detection of some SF, the stellar disc of NGC 4203 is growing at a very low rate and the morphology of the galaxy is unlikely to change significantly in the foreseeable future.

ACKNOWLEDGMENTS

MKY acknowledges a Ph.D. scholarship from The Council of Higher Education of Turkey and is supported by the University of Erciyes.

We would like to thank the GALEX team for their great work to make the data public and available. This work uses observations made with the NASA Galaxy Evolution Explorer. GALEX is operated for NASA by Caltech under NASA contract NAS5-98034. Part of this work is based on observations made with the Spitzer Space Telescope, which is operated by the Jet Propulsion Laboratory (JPL), California Institute of Technology under a contract with NASA. This research has made use of the NASA/IPAC Extragalactic Database (NED) which is operated by JPL, Caltech, under contract with NASA.

REFERENCES

- Adelman-McCarthy J. K. et al., 2007, *ApJS*, 172, 634
 Ahn C. P. et al., 2012, *ApJS*, 203, 21
 Alatalo K. et al., 2013, *MNRAS*, 432, 1796
 Anderson J. M., Ulvestad J. S., 2005, *ApJ*, 627, 674
 Barnes J. E., 2002, *MNRAS*, 333, 481
 Bianchi L., 2011, *Ap&SS*, 335, 51
 Bigiel F., Leroy A., Walter F., Blitz L., Brinks E., de Blok W. J. G., Madore B., 2010, *AJ*, 140, 1194
 Bigiel F., Leroy A., Walter F., Brinks E., de Blok W. J. G., Madore B., Thornley M. D., 2008, *AJ*, 136, 2846
 Bohlin R. C., Savage B. D., Drake J. F., 1978, *ApJ*, 224, 132
 Boissier S. et al., 2012, *A&A*, 545, A142
 Boselli A., Lequeux J., Gavazzi G., 2004, *A&A*, 428, 409
 Bosma A., 1978, PhD thesis, PhD Thesis, Groningen Univ., (1978)
 Burstein D., 1979, *ApJ*, 234, 435
 Burstein D., Krumm N., 1981, *ApJ*, 250, 517
 Calzetti D., 2013, *Star Formation Rate Indicators*, Falc3n-Barroso J., Knapen J. H., eds., p. 419
 Calzetti D. et al., 2005, *ApJ*, 633, 871
 Calzetti D. et al., 2007, *ApJ*, 666, 870
 Cappellari M. et al., 2011, *MNRAS*, 413, 813
 Cappellari M. et al., 2013, *MNRAS*, 432, 1862
 Cortese L., Hughes T. M., 2009, *MNRAS*, 400, 1225
 Crocker A. F., Bureau M., Young L. M., Combes F., 2011, *MNRAS*, 410, 1197
 Davis T. A. et al., 2013, *MNRAS*, 429, 534
 de Vaucouleurs G., de Vaucouleurs A., Corwin, Jr. H. G., Buta R. J., Paturel G., Fouqu3 P., 1991, *Third Reference Catalogue of Bright Galaxies. Volume I: Explanations and references. Volume II: Data for galaxies between 0^h and 12^h . Volume III: Data for galaxies between 12^h and 24^h* . Springer, New York, NY (USA), ISBN 0-387-97552-7
 Di Matteo P., Combes F., Melchior A.-L., Semelin A., 2007, *A&A*, 468, 61
 Donovan J. L. et al., 2009, *AJ*, 137, 5037
 Duc P.-A. et al., 2015, *MNRAS*, 446, 120
 Duc P.-A., Paudel S., McDermid R. M., Cuillandre J.-C., Serra P., Bournaud F., Cappellari M., Emsellem E., 2014, *MNRAS*, 440, 1458
 Engelbracht C. W., Gordon K. D., Rieke G. H., Werner M. W., Dale D. A., Latter W. B., 2005, *ApJ*, 628, L29
 Erwin P., Sparke L. S., 2003, *ApJS*, 146, 299
 Fang J. J., Faber S. M., Salim S., Graves G. J., Rich R. M., 2012, *ApJ*, 761, 23
 Fazio G. G. et al., 2004, *ApJS*, 154, 10
 Kauffmann G. et al., 2007, *ApJS*, 173, 357
 Kelson D. D., Holden B. P., 2010, *ApJ*, 713, L28
 Kormendy J., Bender R., 2012, *ApJS*, 198, 2
 Krajnovi3 D. et al., 2013, *MNRAS*, 432, 1768
 Laurikainen E., Salo H., Buta R., Knapen J. H., 2011, *MNRAS*, 418, 1452
 Leger A., Puget J. L., 1984, *A&A*, 137, L5
 Lelli F., Fraternali F., Sancisi R., 2010, *A&A*, 516, A11
 Lemonias J. J. et al., 2011, *ApJ*, 733, 74
 Leroy A. K., Walter F., Brinks E., Bigiel F., de Blok W. J. G., Madore B., Thornley M. D., 2008, *AJ*, 136, 2782
 Marble A. R. et al., 2010, *ApJ*, 715, 506
 Martin C., GALEX Team, 2005, in *IAU Symposium, Vol. 216, Maps of the Cosmos*, Colless M., Staveley-Smith L., Stathakis R. A., eds., p. 221
 Martini P., Dicken D., Storchi-Bergmann T., 2013, *ApJ*, 766, 121
 McDermid R. M. et al., 2015, *MNRAS*, 448, 3484
 Miller E. D., Knezek P. M., Bregman J. N., 1999, *ApJ*, 510, L95
 Moffett A. J., Kannappan S. J., Baker A. J., Laine S., 2012, *ApJ*, 745, 34
 Morganti R. et al., 2006, *MNRAS*, 371, 157
 Morrissey P. et al., 2007, *ApJS*, 173, 682
 Morrissey P. et al., 2005, *ApJ*, 619, L7
 Oosterloo T. et al., 2010, *MNRAS*, 409, 500
 Oosterloo T. A., Morganti R., Sadler E. M., van der Hulst T., Serra P., 2007, *A&A*, 465, 787
 Pahre M. A., Ashby M. L. N., Fazio G. G., Willner S. P., 2004, *ApJS*, 154, 229

- Pota V. et al., 2013, MNRAS, 428, 389
Rieke G. H. et al., 2004, ApJS, 154, 25
Romanowsky A. J., Douglas N. G., Arnaboldi M., Kuijken K., Merrifield M. R., Napolitano N. R., Capaccioli M., Freeman K. C., 2003, Science, 301, 1696
Salim S. et al., 2009, ApJ, 700, 161
Salim S., Fang J. J., Rich R. M., Faber S. M., Thilker D. A., 2012, ApJ, 755, 105
Salim S., Rich R. M., 2010, ApJ, 714, L290
Salim S. et al., 2007, ApJS, 173, 267
Sandage A., Freeman K. C., Stokes N. R., 1970, ApJ, 160, 831
Sarzi M. et al., 2006, MNRAS, 366, 1151
Sault R. J., Teuben P. J., Wright M. C. H., 1995, in Astronomical Society of the Pacific Conference Series, Vol. 77, Astronomical Data Analysis Software and Systems IV, Shaw R. A., Payne H. E., Hayes J. J. E., eds., p. 433
Schlegel D. J., Finkbeiner D. P., Davis M., 1998, ApJ, 500, 525
Sellgren K., 1984, ApJ, 277, 623
Serra P. et al., 2012, MNRAS, 422, 1835
Serra P. et al., 2014, MNRAS, 444, 3388
Serra P., Trager S. C., Oosterloo T. A., Morganti R., 2008, A&A, 483, 57
Shapiro K. L. et al., 2010, MNRAS, 402, 2140
Spitzer, Jr. L., Baade W., 1951, ApJ, 113, 413
Thilker D. A. et al., 2010, ApJ, 714, L171
Trager S. C., Faber S. M., Worthey G., González J. J., 2000, AJ, 119, 1645
van den Bergh S., 1976, ApJ, 206, 883
van Driel W., van Woerden H., 1991, A&A, 243, 71
van Driel W., van Woerden H., Schwarz U. J., Gallagher I. J. S., 1988, A&A, 191, 201
Vladilo G., 2002, A&A, 391, 407
Walter F., Brinks E., de Blok W. J. G., Bigiel F., Kennicutt, Jr. R. C., Thornley M. D., Leroy A., 2008, AJ, 136, 2563
Weijmans A.-M. et al., 2014, MNRAS, 444, 3340
Welch G. A., Sage L. J., 2003, ApJ, 584, 260
Werner M. W. et al., 2004, ApJS, 154, 1
Wu H., Cao C., Hao C.-N., Liu F.-S., Wang J.-L., Xia X.-Y., Deng Z.-G., Young C. K.-S., 2005, ApJ, 632, L79
Wyder T. K. et al., 2007, ApJS, 173, 293
Yi S. K. et al., 2005, ApJ, 619, L111
Young L. M., 2002, AJ, 124, 788
Young L. M. et al., 2011, MNRAS, 414, 940